Ferromagnetism in van der Waals compound $MnSb_{1.8}Bi_{0.2}Te_4$

Yangyang Chen,[1,3] Ya-Wen Chuang,[1] Seng Huat Lee,[1,2] Yanglin Zhu,[1,2] Kevin Honz,[1] Yingdong Guan,[1] Yu Wang,[1,2] Ke Wang,[5] Zhiqiang Mao,[1,2] Jun Zhu,[1,*] Colin Heikes,[4] P. Quarterman,[4] Pawel Zajdel,[6] Julie A. Borchers,[4] and William Ratcliff II[4,7]

[1]*Department of Physics, The Pennsylvania State University, University Park, Pennsylvania 16802, USA*
[2]*2D Crystal Consortium, Materials Research Institute, The Pennsylvania State University, University Park, Pennsylvania 16802, USA*
[3]*International Center for Quantum Materials, School of Physics, Peking University, Beijing 100871, People's Republic of China*
[4]*NIST Center for Neutron Research, NIST, Gaithersburg, Maryland 20899, USA*
[5]*Materials Characterization Laboratory, Materials Research Institute, The Pennsylvania State University, University Park, Pennsylvania 16802, USA*
[6]*Institute of Physics, University of Silesia, ul. 75 Pulku Piechoty 1, 41-500, Chorzow, Poland*
[7]*Department of Materials Science and Engineering, University of Maryland, College Park, Maryland 20742, USA*

(Received 19 October 2019; revised manuscript received 20 February 2020; accepted 28 April 2020; published 11 June 2020)

The intersection of topology and magnetism represents a new playground to discover novel quantum phenomena and device concepts. In this work, we show that under certain synthetic conditions, a van der Waals single-crystalline compound $MnSb_{1.8}Bi_{0.2}Te_4$ exhibits a net ferromagnetic state with a Curie temperature of 26 K, in contrast to the fully compensated antiferromagnetic order observed previously for other members of the $Mn(Sb,Bi)_2Te_4$ family. We employ magneto-transport, bulk magnetization, x-ray and neutron scattering studies to illustrate the structural, magnetic, and electrical properties of $MnSb_{1.8}Bi_{0.2}Te_4$. Our structural analyses reveal considerable Mn-Sb site mixing and suggest a recently proposed mechanism, where Mn occupying the Sb site mediates a ferromagnetic coupling between Mn layers [Murakami *et al.*, Phys. Rev. B **100**, 195103 (2019)], could be at play. Close comparisons made to an antiferromagnetic compound $MnSb_2Te_4$ illustrate the subtle magnetic interactions of the system and the important role played by local chemistry. The appearance of an unusual anomalous Hall effect in $MnSb_{1.8}Bi_{0.2}Te_4$ at low temperatures hints at a magnetic ground state different from other members of this family. Our results are an important step in the synthesis and understanding of magnetism in materials with topological characteristics.

DOI: 10.1103/PhysRevMaterials.4.064411

I. INTRODUCTION

A central theme of contemporary condensed matter research explores the notion of topology and symmetry to generate novel quantum phenomena [1]. A good example is the quantum anomalous Hall effect (QAHE) found in magnetic topological insulators $Cr_{0.15}(Bi, Sb)_{1.85}Te_3$, where magnetism introduced by Cr doping breaks the time reversal symmetry and gives rise to robust chiral edge states that can carry current ballistically without the need of an external magnetic field [2,3]. Chiral magnetic textures such as skyrmions are another good example [4–6]. The generation of spin chirality requires the breaking of crystalline inversion symmetry, which can be achieved in bulk materials [7–9] or in heterostructures that combine ferromagnetism (FM) with strong spin-orbit coupling [10–14]. Magnetism and heterostructures in the van der Waals (vdW) geometry provide another powerful natural platform to explore magnetic anisotropy and interface effect, with the added benefit of electric-field control for potential device applications [15–20].

Recent research activities have identified $Mn(Bi,Sb)_2Te_4$, a vdW magnetic family with strong spin-orbit coupling, to be promising candidates in realizing the QAHE above dilution refrigerator temperatures [21–32]. $Mn(Bi,Sb)_2Te_4$ can be regarded as consisting of a Mn-Te layer inserted into the quintuple layer of $(Sb,Bi)_2Te_3$ [Fig. 1(a)]. Here moments carried by an ordered Mn layer can create an internal magnetic field without introducing random disorder. In the most studied compound $MnBi_2Te_4$, the interlayer Mn coupling was found to be *A*-type antiferromagnetic (AFM) [21–23,30,31,33–35]. The AFM ground state was also favored in other compositions of the compound family [31] with the exception of a recent report of ferrimagnetism in polycrystalline $MnSb_2Te_4$ [36]. Few-layer devices exfoliated from antiferromagnetic $MnBi_2Te_4$ crystals show the QAHE effect [24]. A ferromagnetic bulk can stabilize the effect at higher temperature and open the door to other interesting possibilities such as type-II Weyl semimetals with broken time reversal symmetry [36,37].

In this work, we show that under certain synthetic conditions, single-crystalline $MnSb_{1.8}Bi_{0.2}Te_4$ can be stabilized into a phase with a net ferromagnetic moment and a Curie temperature of $T_C = 26$ K. We present transport, magnetometry, and neutron diffraction measurements that

*jxz26@psu.edu

illustrate the properties of this state, which we denote as the "FM" state. Refinements of x-ray and neutron diffraction data reveal considerable Mn-Sb site mixing, which supports a recent Mn layer to Mn layer ferromagnetic coupling mechanism discussed in Ref. [36]. Interestingly, our sample also exhibits a sizable unconventional anomalous Hall effect that signals the possibility of additional magnetic structure at very low temperatures. Further understanding of the rich magnetic orders the $Mn(Bi,Sb)_2Te_4$ family exhibits and their correlation with local chemistry opens up possibilities of engineering magnetic and topological phenomena in this vdW family with potential prospects in device applications.

II. EXPERIMENTAL METHODS

$MnSb_{1.8}Bi_{0.2}Te_4$ single crystals exhibiting the FM state were synthesized using a flux method. A mixture of high-purity Mn powder (99.95%), Bi shot (99.999%), antimony shot (99.9999%) and Te ingot (99.9999+%) with the molar ratio of Mn:Sb:Bi:Te = 1:9:1:16 was loaded into an Al_2O_3 crucible and sealed in an evacuated quartz tube. The mixture was heated up to 900 °C for 12 h to promote homogeneous melting and then slowly cooled down to 595 °C at a rate of 2 °C/h and dwelled at this temperature for 24 h. It is then further cooled down to 400 °C within 3 h and then immediately heated back to 625 °C in 1 h and dwelled at this temperature for another 2 h. We then move the sample quickly from the furnace to a centrifuge to remove the excess flux before letting it cool down in the centrifuge. The treatment of cooling down the melt from 900 to 400 °C before going back to 625 °C is critical to the synthesis of the FM state in $MnSb_{1.8}Bi_{0.2}Te_4$. Cooling the melt directly to 625 °C without this step leads to an AFM ground state similar to prior results [31]. A $MnSb_{1.85}Bi_{0.15}Te_4$ crystal synthesized via this method displays very similar Curie temperature and saturation moment to the $MnSb_{1.8}Bi_{0.2}Te_4$ discussed in the main text (see Fig. S3 of the Supplemental Material (SM) [38]). We also attempted synthesizing $MnSb_2Te_4$ crystals using the same method, but obtained only crystals exhibiting the AFM ground state. $MnSb_2Te_4$ crystals studied here were prepared using a flux method similar to that used in Ref. [31]. X-ray diffraction (XRD) and scanning transmission electron microscopy measurements confirm the septuple-layer rhombohedral structural phase in both materials. Measurements presented in the main text are obtained on crystals and exfoliated flakes with greater than 95% purity in the primary $Mn(Sb,Bi)_2Te_4$ phase (see Figs. S1 and S2 of the Supplemental Material [38]). Powdered polycrystalline samples of both $MnSb_{1.8}Bi_{0.2}Te_4$ and $MnSb_2Te_4$ are grown with the same methodologies and are verified to have the same magnetic ground states as their single-crystal counterparts. They are used for neutron powder diffraction (NPD) studies. Rietveld analysis on the NPD was performed using a combination of the FULLPROF and GSAS-II programs (see details in Sec. S1 of the SM [38–41]). Figure 1(a) illustrates a schematic sideview of the layer stacking in the $Mn(Bi,Sb)_2Te_4$ family. Micrometer-sized flakes are exfoliated from selected crystals and transferred using a polypropylene carbonate stamp to prepatterned electrodes inside a glovebox filled with argon gas. The finished device is covered with a droplet of Poly(Methyl MethAcrylate) before being transferred to a cryostat. Figure 1(b) shows an optical image of a typical Hall bar device. Flakes of similar color tone measure 100–300 nm in thickness in an atomic force microscope. Transport measurements are performed in a pumped ^{4}He cryostat with a magnetic field up to 9 T using standard low-frequency techniques. Magnetometry measurements are performed in a superconducting quantum interference device magnetometer from 2 to 300 K. Single-crystal elastic neutron scattering measurements are performed using the BT-4 triple-axis spectrometer (TAS) and NPD measurements were made on the BT-1 powder diffractometers at the NIST Center for Neutron Research (NCNR). The BT-1 measurements were made using 60′ collimation with both Cu(311) and Ge(311) monochromators. TAS measurements were taken with an instrument configuration of open-pg-pg-40′-s-pg-40′-100′ where pg refers to pyrolytic graphite.

III. RESULTS AND DISCUSSION

Figure 1(c) plots the Hall resistance $R_{xy}(H)$ obtained on a $MnSb_{1.8}Bi_{0.2}Te_4$ device. A small R_{xx} component is removed from the data though an asymmetrization step that averages the upsweep of $R_{xy}(H)$ and the downsweep of $-R_{xy}(-H)$. Measurements were taken at a series of fixed temperatures ranging from 2 to 60 K. Traces plotted here represent the typical behavior in different temperature ranges. As the $T = 60$ K trace shows, $R_{xy}(H)$ is a straight line from −9 to 9 T at high temperatures. An anomalous Hall effect starts to develop at $T < 46$ K, where the slope dR_{xy}/dH taken at $R_{xy} = 0$ (illustrated by a green dashed line for the $T = 2$ K upsweep trace) becomes larger than the slope taken at high field (a black dashed line in the inset). The difference of the two originates from a nonzero magnetization (M) of the sample since $R_{xy}(H) = R_0H + R_sM$ [42]. At sufficiently high field where M saturates, the slope dR_{xy}/dH yields the normal Hall coefficient $R_0 = 1/ne$. R_0 follows a $\cos\theta$ dependence as the external field tilts away from the c axis of the crystal (Fig. S4), which confirms the two-dimensional nature of the mobile carriers and yields a hole carrier density of $n_h = 6.3 \times 10^{15}/\text{cm}^2$. This translates to a doping level of $\sim 10^{13}/\text{cm}^2$ per septuple layer and puts the Fermi level in the bulk valence band of $MnSb_{1.8}Bi_{0.2}Te_4$ [31]. R_0 is approximately T independent, as demonstrated in Fig. S4 of the SM [38]. In contrast, the slope dR_{xy}/dH taken at $R_{xy} = 0$, called the low-field slope from now on, increases rapidly with decreasing temperature and reaches a broad maximum around 12–20 K. Its T dependence is plotted in Fig. 2(a) as magenta circles. Similar measurements are performed on a $MnSb_2Te_4$ device and the results are plotted as blue squares.

In addition to the anomalous Hall effect, $R_{xy}(H)$ becomes hysteretic at temperatures below ∼23 K. Data at 2 and 15 K are plotted to show the two different shapes of the hysteresis loop. Hysteresis is also observed in bulk magnetization measurements of the parent $MnSb_{1.8}Bi_{0.2}Te_4$ crystal. Figure 1(d) plots the $M(H)$ data at $T = 2$ K, from which we extracted a remnant magnetization of $M_0 = 0.6\,\mu_B$/Mn, a coercive field of $H_c = 310$ Oe, and a saturated M of $1.8\,\mu_B$/Mn [inset of Fig. 1(d)]. Both the H_c and $R_{xy}^{H=0}$ decrease with increasing temperature and vanish at $T > 23$ K, supporting the establish-

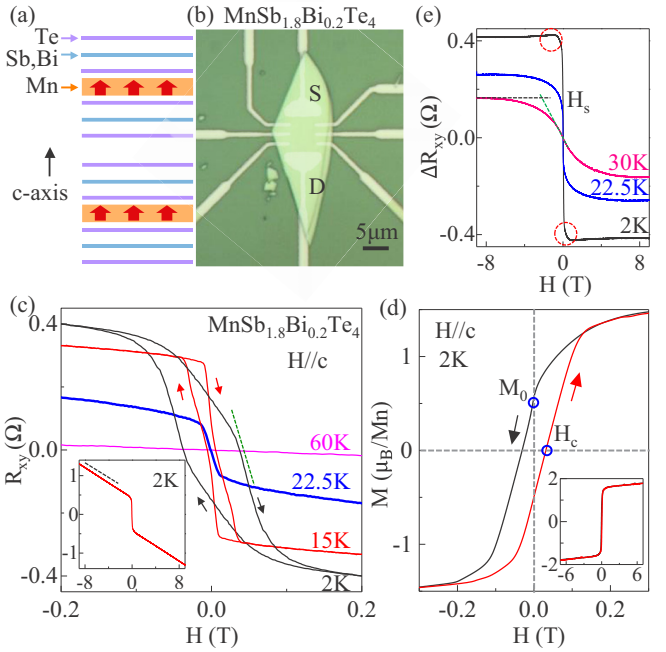

FIG. 1. (a) Schematic stacking order of $Mn(Sb,Bi)_2Te_4$. (b) An optical image of a typical $MnSb_{1.8}Bi_{0.2}Te_4$ device in a Hall bar geometry. (c) The Hall resistance $R_{xy}(H)$ on a $MnSb_{1.8}Bi_{0.2}Te_4$ device at selected temperatures as labeled in the plot. Arrows indicate the field-sweep direction. The green dashed line illustrates the low-field slope dR_{xy}/dH taken at $R_{xy} = 0$. The inset shows the full-range down sweep of $R_{xy}(H)$ at 2 K. The black dashed line illustrates the high-field slope dR_{xy}/dH. (d) $M(H)$ of a $MnSb_{1.8}Bi_{0.2}Te_4$ crystal. The coercive field $H_c = 310$ Oe. $1\,\mathrm{Oe} = (1000/4\pi)\,\mathrm{A/m}$. The remnant magnetization $M_0 = 0.6\,\mu_B$/Mn. Inset: $M(H)$ to 7 T showing a saturated magnetization of $\sim 1.8\,\mu_B$/Mn. (e) The anomalous Hall component $\Delta R_{xy}(H)$ for the device shown in (b) at selected temperatures. $\Delta R_{xy}(H)$ is obtained by subtracting the normal Hall contribution $R_0 H$ from the measured $R_{xy}(H)$. The dashed lines illustrate the process of obtaining the saturation field H_s for the $T = 30$ K trace. Fig. S5 of the SM illustrates the determination of H_s at $T < 22.5$ K, when hysteresis is present [38]. Up and down sweeps produce the same H_s.

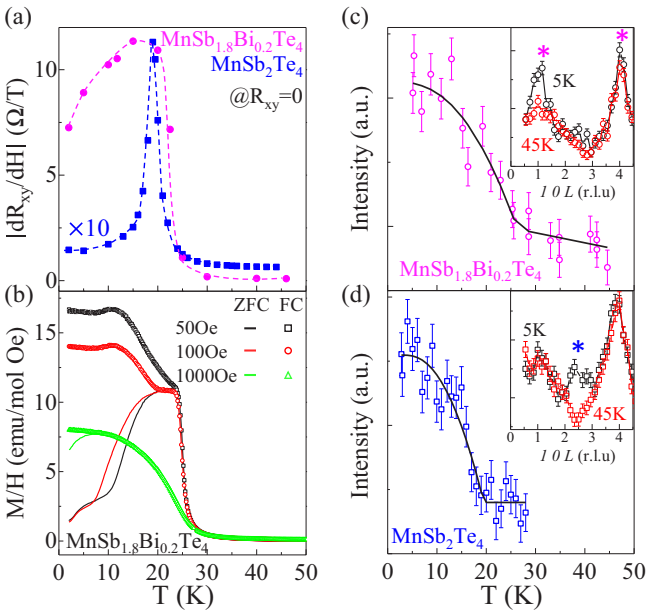

FIG. 2. (a) The low-field slope dR_{xy}/dH as a function of temperature in $MnSb_{1.8}Bi_{0.2}Te_4$ (magenta circles) and $MnSb_2Te_4$ (blue squares). The dashed lines are a guide to the eye. (b) The temperature-dependent magnetic susceptibility M/H of a $MnSb_{1.8}Bi_{0.2}Te_4$ sample measured at three external fields $H = 50$, 100, and 1000 Oe under both ZFC and FC conditions as labeled in the graph. $H \parallel c$. The molar magnetic susceptibility $\chi_m = MV_m/H$, where V_m is the volume per gram mole. $1\,\mathrm{emu/(mol\,Oe)} = 4\pi \times 10^{-6}\,\mathrm{m^3/mol}$. (c), (d) The main panels show the temperature-dependent elastic neutron scattering centered at the (*1 0 1*) reflection in $MnSb_{1.8}Bi_{0.2}Te_4$ (c) and the (*1 0 2.5*) reflection in $MnSb_2Te_4$ (d). Mean-field fits (solid lines) yield $T_C = 26.3$ K in (c) and $T_N = 19.5$ K in (d). The insets show scans along the (*1 0 L*) direction at 5 and 45 K with the * symbol marking the (*1 0 1*) and (*1 0 4*) reflections in (c) and the (*1 0 2.5*) reflection in (d). Larger-range scans from (*1 0 4*) to (*1 0 −4*) on both compounds are shown in Fig. S7 to show a clear increase of the (*1 0 4*) peak with decreasing temperature and the lack of twinning in the $MnSb_{1.8}Bi_{0.2}Te_4$ samples [38]. Error bars in (c) and (d) represent one standard deviation.

ment of the FM state in this temperature vicinity (see Fig. S6 of the Supplemental Material [38]).

To further explore the magnetic properties of $MnSb_{1.8}Bi_{0.2}Te_4$, we plot in Figs. 2(a) and 2(b) the T-dependent magnetic susceptibility $\chi(T)$, extracted from the low-field slope of the Hall resistance dR_{xy}/dH and DC magnetometry measurements, respectively. In a magnetic system, the low-field slope dR_{xy}/dH includes the contribution from the out-of-plane magnetic susceptibility $\chi = dM/dH$. In Fig. 2(a), dR_{xy}/dH ascends rapidly at $T \sim 25$ K, reaches a maximum value of 11 Ω/T around 12–20 K, which is more than 100 times larger than the normal Hall coefficient $R_0 = 0.1\,\Omega$/T of this device, before dropping again at lower temperatures. In other words, the low-field slope dR_{xy}/dH is dominated by the magnetic response of the system and effectively measures the $\chi(T)$ of the microscope device. The magnetometry studies conducted on bulk crystals tell a similar story. Figure 2(b) plots the temperature-dependent linear susceptibility $M/H(T)$ obtained under both zero-field-cooling (ZFC) and several field-cooling (FC) conditions using several different fields as labeled in the plot. The 50 Oe ZFC data (solid black line) strongly resemble the low-field slope dR_{xy}/dH shown in Fig. 2(a), suggesting that our samples behave homogeneously from the μm to the mm length scale. Both support the onset of a FM order at a Curie temperature of $T_C \sim 26$ K obtained by fitting the neutron scattering data below. At $T < 12$ K, both the low-field slope dR_{xy}/dH and the low-field ZFC M/H data show a pronounced drop that deviates from a conventional FM. More complex magnetic phases may emerge in this temperature range [34,43–45]. We aim to understand its nature with additional measurements and analyses [46].

Figures 2(c) and 2(d) compare neutron scattering results obtained on our $MnSb_{1.8}Bi_{0.2}Te_4$ and $MnSb_2Te_4$ single crystals. Upon cooling, the (*1 0 1*) and (*1 0 4*) nuclear reflection

peaks in $MnSb_{1.8}Bi_{0.2}Te_4$ gained intensity with no peak appearing at the (*1 0 2.5*) position (Fig. 2(c) inset and a larger range scan from (*1 0 −4*) to (*1 0 4*) in Fig. S7 of the SM [38]). In contrast, the (*1 0 2.5*) peak appeared at low temperatures in our $MnSb_2Te_4$ sample while the amplitude of the nuclear reflections remained unchanged (Fig. 2(d) inset and a larger range scan from (*1 0 −4*) to (*1 0 4*) in Fig. S7 of the SM [38]). The (*1 0 2.5*) peak is associated with the development of the *A*-type AFM phase in $MnBi_2Te_4$ in previous reports [30,32]. The neutron data clearly indicate a different magnetic order in our samples, that is, AFM in $MnSb_2Te_4$ and FM in $MnSb_{1.8}Bi_{0.2}Te_4$. Mean-field fits to the temperature-dependent scattering amplitude at the (*1 0 1*) and (*1 0 2.5*) positions yield a Curie temperature of $T_C \sim 26$ K and a Néel temperature of $T_N \sim 20$ K for the $MnSb_{1.8}Bi_{0.2}Te_4$ and $MnSb_2Te_4$ samples, respectively. Further, we show in Fig. 2(a) the low-field slope dR_{xy}/dH we obtained on a $MnSb_2Te_4$ device (solid blue squares). It is consistent with an AFM phase with $T_N \sim 19.5$ K, and is in excellent agreement with previous susceptibility measurements of this material [31].

Diverse observations including the FM and AFM order we identified in our $MnSb_{1.8}Bi_{0.2}Te_4$ and $MnSb_2Te_4$ crystals, respectively, the literature results of mostly AFM order in the majority of the $Mn(Bi,Sb)_2Te_4$ crystals synthesized [21,23,30,31,33], and a very recent report of a ferrimagnetic ground state with $T_C \sim 25$ K in polycrystalline $MnSb_2Te_4$ [36] all together paint a much more nuanced picture than anticipated from initial calculations of this compound family. The intrinsic AFM or FM coupling between adjacent Mn layers competes closely in energy in Sb-rich compositions [31,33]. In Ref. [36], the authors showed that site mixing between Mn and Sb sites can alter the interlayer Mn-Mn exchange coupling from AFM to FM via a ferrimagnetic configuration that aligns Mn moment occupying the Sb site in the opposite direction. Through the refinement of x-ray and NPD data, we have also found a considerable amount of antisite defects in our $MnSb_{1.8}Bi_{0.2}Te_4$ and $MnSb_2Te_4$ samples, with approximately 41(1)% and 26(1)% of Mn occupying nominal (Bi,Sb) sites in $MnSb_2Te_4$ and $MnSb_{1.8}Bi_{0.2}Te_4$, respectively. The inclusion of Bi seems to suppress the presence of the antisite defects, which is consistent with the significantly fewer antisite defects (3%) and the universal AFM ground state found in the end compound $MnBi_2Te_4$ [32]. A full discussion of the local and long-ranged defects observed in our samples can be found in Sec. S1 of the SM [38,47]. In the literature, Mn-doped Bi_2Te_3 is known to have a FM ground state [48–50]. Samples studied here are screened by XRD to have less than 5% intergrowth of the $(Sb,Bi)_2Te_3$ phase. In addition, we have explicitly tested the behavior of a flake exfoliated from a crystal with significant secondary Bi_2Te_3 intergrowth. The results are presented in Fig. S11 of the SM [38]. This device exhibits a Curie temperature of ∼ 11 K and its transport and magnetotransport behavior closely resembles that of Mn-doped Bi_2Te_3 [48–50], but are very different from that of the $MnSb_{1.8}Bi_{0.2}Te_4$ and $MnSb_2Te_4$ devices. No excess anomalous Hall signal discussed in Fig. 4 was observed. These results rule out the possibility of an FM state originating solely from the ferromagnetic coupling of Mn occupying the Sb site.

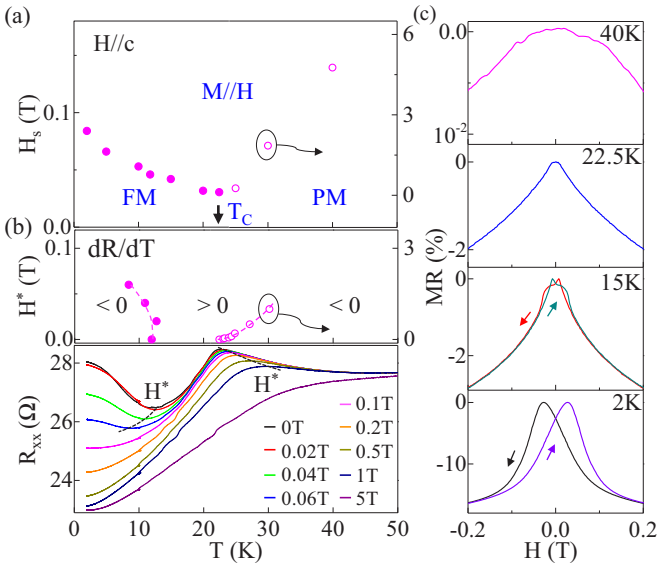

FIG. 3. (a) Moment saturation field H_s vs T in $MnSb_{1.8}Bi_{0.2}Te_4$ obtained from $\Delta R_{xy}(H)$ data shown in Fig. 1(e) and Fig. S5. Solid symbols are data below T_C. Open symbols are data above T_C and use the right axis. (b) Lower panel: Temperature-dependent magnetoresistance $R_{xx}(T)$ taken at fixed magnetic field as labeled in the plot. The black dashed lines divide the curves into three regions according to the sign of dR/dT. The boundary points are plotted in the upper panel of (b). The symbols follow the notation of (a). (c) Normalized magnetoresistance $\mathrm{MR} = [R_{xx}(H) - R_{xx}(0)]/R_{xx}(0) \times 100\%$ at selected temperatures. Arrows indicate field-sweep direction. Note the change of the *y* scale in different panels.

The different magnetic orders exhibited by our samples and others' highlight the sensitivity of the magnetic interactions of the system to the details of the local defect chemistry. As described in the Methods section, we are able to grow $MnSb_{1.8}Bi_{0.2}Te_4$ crystals that are either FM or AFM using different thermal treatments before quenching, which could conceivably lead to different local defect chemistry that supports different magnetic orders. Further understanding of this process and the identification of synthesis conditions that lead to FM order in a wide range of alloy compositions will be an important goal of future studies. In the remainder of the paper, we continue to describe the properties of $MnSb_{1.8}Bi_{0.2}Te_4$ samples that display the FM characteristics, focusing on its transport characteristics and the appearance of an excess anomalous Hall signal at yet lower temperatures of $T < 12$ K.

The sensitivity of R_{xy} to the magnitude of M enables us to determine the saturation field H_s and construct an H_s-T phase diagram. To do this we first determine the anomalous Hall signal $\Delta R_{xy}(H) = R_{xy}(H) - R_0(H)$. The results for the device shown in Fig. 1(b) at several temperatures are shown in Fig. 1(e). The saturation field H_s is defined as the field at which the extension of the slope at $R_{xy} = 0$ reaches the saturated value of ΔR_{xy}, as illustrated by the dashed lines for the $T = 30$ K trace. Figure S5 of the SM illustrates the process of determining H_s at low temperature when hysteresis is present [38]. Figure 3(a) plots the resulting H_s-T diagram. H_s reaches a minimum of 0.030 T near T_C. The onset of a hysteresis loop leads to a small increase of H_s with decreasing

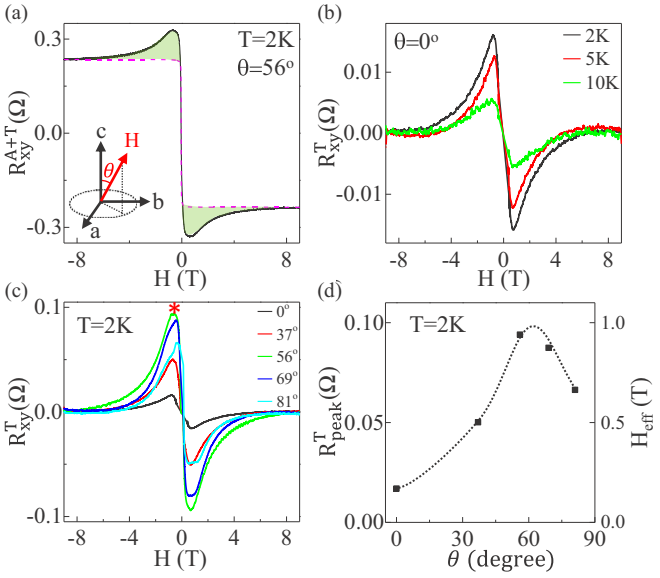

FIG. 4. The excess anomalous Hall effect in $MnSb_{1.8}Bi_{0.2}Te_4$. (a) $R_{xy}^{A+T}(H)$, which is the same as $\Delta R_{xy}(H)$ in Fig. 1(e) at $T = 2\,\mathrm{K}$ and with a tilt angle $\theta = 56^\circ$ as illustrated in the inset. The magenta dashed line is a Langevin fit to the anomalous Hall effect with an uncertainty of $0.9\,\mathrm{m\Omega}$. The area shaded in green indicates the excess Hall effect contribution R_{xy}^{T}. (b) $R_{xy}^{T}(H)$ at $\theta = 0^\circ$ and $T = 2$, 5, and 10 K. Data obtained from up and down sweeps are shifted horizontally to coincide at $H = 0$. (c) $R_{xy}^{T}(H)$ at $T = 2\,\mathrm{K}$ and selected tilt angle θ. R_{peak}^{T} is marked by the * symbol. (d) The angular dependence of R_{peak}^{T} at $T = 2\,\mathrm{K}$. The right axis labels the effective magnetic field $H_{\mathrm{eff}} = R_{\mathrm{peak}}^{T}/R_0$.

temperature at $T < T_C$. Remarkably, at low temperature, H_s is only 0.084 T in $MnSb_{1.8}Bi_{0.2}Te_4$, in comparison to 0.42 T in $MnSb_2Te_4$ (Fig. S9 of the SM [38]) and more than 7 T in $MnBi_2Te_4$ (Fig. S10 of the SM [38]), despite similar ordering temperatures of ∼20 K in all three materials. This observation strongly attests to the FM order in $MnSb_{1.8}Bi_{0.2}Te_4$. The small H_s here is associated with the alignment of the FM domains in an external field, rather than the spin-flop transition of individual Mn moment. In addition, we see that the anomalous Hall effect extends into the paramagnetic phase [open circles in Fig. 3(a)], indicating FM fluctuations are already important at $T \geqslant T_C$.

Next, we demonstrate the impact of magnetic order on the transport characteristics of $MnSb_{1.8}Bi_{0.2}Te_4$. Figure 3(b) plots $R_{xx}(T)$ traces taken at a series of fixed magnetic fields. We track the sign change of dR/dT as a function of T and H and plot the results on an H-T map, similar to the H_s-T diagram shown in Fig. 3(a). At temperatures above ∼50 K, $R_{xx}(T)$ exhibits the expected metallic T dependence, i.e., $dR/dT > 0$ with no dependence on the magnetic field. An expanded $R_{xx}(T)$ from 2 to 100 K is given in Fig. S8 of the SM [38]. As T approaches T_C, strong spin fluctuations lead to a slightly insulating T dependence, i.e., $dR/dT < 0$, similar to the situation in $MnBi_2Te_4$ [30]. A positive dR/dT is found again when the moments align spontaneously or under a sufficiently large external field, likely due to the reduction of magnetic scatterings that involve a spin-flip/flop. The onset of another insulatorlike regime at $T < 12\,\mathrm{K}$ coincides with the drop of χ in Fig. 2(a), and the onset of an excess anomalous Hall signal in Fig. 4. We are working to understand its origin.

Figure 3(c) plots the normalized magnetoresistance (MR) of a $MnSb_{1.8}Bi_{0.2}Te_4$ device at selected temperatures. In $MnSb_{1.8}Bi_{0.2}Te_4$, MR is always negative. Its magnitude increases with decreasing temperature and becomes hysteretic with the onset of the FM order. Alignment of all moments in an external field results in a large reduction of nearly 20% at low temperature. Comparing to similar measurements on $MnSb_2Te_4$ and $MnBi_2Te_4$ (Figs. S9 and S10 of the SM [38]), we see that electrical transport in Sb-rich compositions is much more influenced by the magnetic order, likely because the Mn orbitals are located in the valence band and couple more closely to the hole carriers in $MnSb_{1.8}Bi_{0.2}Te_4$ and $MnSb_2Te_4$ [31,33].

Finally, we report the appearance of an excess anomalous Hall signal in $MnSb_{1.8}Bi_{0.2}Te_4$ that is beyond the conventional AHE. This signal concentrates in the circled areas in the $\Delta R_{xy}(H)$ plot shown in Fig. 1(e). Following the literature [11,13,14], we fit the conventional AHE component R_{xy}^{A} with a Langevin function [magenta dashed line in Fig. 4(a)] and use R_{xy}^{T} to denote the excess signal (green shaded area). Figures 4(b) and 4(c) plot $R_{xy}^{T}(H)$ obtained at several temperatures and different tilt angles of the external field, respectively. The raw $\Delta R_{xy}(H)$ plots are given in Fig. S12 of the SM [38]. The magnitude of $R_{xy}^{T}(H)$ decreases rapidly with increasing temperature and approaches the fitting uncertainty ($\pm 0.9\,\mathrm{m\Omega}$) at $T > 10\,\mathrm{K}$. The signal peaks at $H \sim \pm 0.7\,\mathrm{T}$ and persists to several tesla. Figure 4(d) plots the angle dependence of the peak value R_{peak}^{T} at $T = 2\,\mathrm{K}$. $R_{\mathrm{peak}}^{T}(\theta)$ is nonmonotonic and reaches a maximum of 0.1 Ω around θ∼60°. The value corresponds to a fictitious field of $H_{\mathrm{eff}} = R_{\mathrm{peak}}^{T} ne \sim 1\,\mathrm{T}$; i.e., the excess anomalous Hall signal in our $MnSb_{1.8}Bi_{0.2}Te_4$ sample has considerable strength.

This intriguing excess anomalous Hall signal points to excess Berry curvature of the material, which disappears with increasing magnetic field. The room-temperature crystal structure of $Mn(Sb,Bi)_2Te_4$ is centrosymmetric, which does not allow for a Dzyaloshinskii-Moriya interaction (DMI) term in the Hall effect [4–9]. We have not identified a clear symmetry-lowering structural transition at low temperatures though this possibility cannot be ruled out. Excess Berry curvature can also occur in systems with noncollinear, frustrated, or spatially modulated magnetic textures such as clustered spin glass, frustrated magnets, or noncollinear AFMs [51–53]. Our refinement analysis has revealed considerable Mn-Sb site mixing. The second magnetic sublattice produced by Mn occupying the Sb sites could conceivably play a role in generating a noncollinear magnetic structure. Our ongoing work seeks to further examine this possibility.

IV. CONCLUSION

In summary, we combine electrical transport, bulk magnetometry, and neutron diffraction studies to show evidence of a ferromagnetic ground state with a Curie temperature of 26 K in $MnSb_{1.8}Bi_{0.2}Te_4$. Our work is an encouraging step towards realizing a ferromagnetic topological insulator. Its vdW geometry opens up possibilities of forming heterostructures and gate tuning. Studies that illuminate the synthesis conditions of

different magnetic phases in the $Mn(Sb,Bi)_2Te_4$ family will greatly facilitate future explorations of their topological and magnetic properties.

ACKNOWLEDGMENTS

Y.C., Y-W.C., K.H., and J.Z. are supported by NSF through Grant NSF-DMR-1708972. Y.C. also acknowledges support by the China Scholarship Council. Support for crystal growth and characterization was provided by the National Science Foundation through the Penn State 2D Crystal Consortium-Materials Innovation Platform (2DCC-MIP) under NSF Cooperative Agreement DMR-1539916. Z.Q.M. also acknowledges the support of NSF-DMR-1707502. We thank Xia Hong and Cui-Zu Chang for helpful discussions. P. Z. would like to thank Professor J. Kusz for help with single-crystal measurements and the support of NIST through the Guest Researcher Program. We acknowledge useful contributions by Sergiy Gladchenko for the development of sample environment for the experiments at the NCNR.

[1] M. Z. Hasan and C. L. Kane, Colloquium: Topological insulators, Rev. Mod. Phys. **82**, 3045 (2010).

[2] C.-Z. Chang, J. Zhang, X. Feng, J. Shen, Z. Zhang, M. Guo, K. Li, Y. Ou, P. Wei, L.-L. Wang, Z.-Q. Ji, Y. Feng, S. Ji, X. Chen, J. Jia, X. Dai, Z. Fang, S.-C. Zhang, K. He, Y. Wang, L. Lu, X.-C. Ma, and Q.-K. Xue, Experimental observation of the quantum anomalous Hall effect in a magnetic topological insulator, Science **340**, 167 (2013).

[3] C.-X. Liu, S.-C. Zhang, and X.-L. Qi, The quantum anomalous Hall effect: Theory and experiment, Ann. Rev. Condens. Matter Phys. **7**, 301 (2016).

[4] N. Nagaosa and Y. Tokura, Topological properties and dynamics of magnetic skyrmions, Nat. Nanotechnol. **8**, 899 (2013).

[5] A. Fert, N. Reyren, and V. Cros, Magnetic skyrmions: Advances in physics and potential applications, Nat. Rev. Mater. **2**, 17031 (2017).

[6] Y. Taguchi, Y. Oohara, H. Yoshizawa, N. Nagaosa, and Y. Tokura, Spin chirality, Berry phase, and anomalous Hall effect in a frustrated ferromagnet, Science **291**, 2573 (2001).

[7] A. Neubauer, C. Pfleiderer, B. Binz, A. Rosch, R. Ritz, P. G. Niklowitz, and P. Boni, Topological Hall Effect in the A Phase of MnSi, Phys. Rev. Lett. **102**, 186602 (2009).

[8] X. Z. Yu, N. Kanazawa, Y. Onose, K. Kimoto, W. Z. Zhang, S. Ishiwata, Y. Matsui, and Y. Tokura, Near room-temperature formation of a skyrmion crystal in thin-films of the helimagnet FeGe, Nat. Mater. **10**, 106 (2011).

[9] S. X. Huang and C. L. Chien, Extended Skyrmion Phase in Epitaxial FeGe (111) Thin Films, Phys. Rev. Lett. **108**, 267201 (2012).

[10] S. Heinze, K. von Bergmann, M. Menzel, J. Brede, A. Kubetzka, R. Wiesendanger, G. Bihlmayer, and S. Blügel, Spontaneous atomic-scale magnetic skyrmion lattice in two dimensions, Nat. Phys. **7**, 713 (2011).

[11] J. Matsuno, N. Ogawa, K. Yasuda, F. Kagawa, W. Koshibae, N. Nagaosa, Y. Tokura, and M. Kawasaki, Interface-driven topological Hall effect in $SrRuO_3$-$SrIrO_3$ bilayer, Sci. Adv. **2**, e1600304 (2016).

[12] J. Jiang, D. Xiao, F. Wang, J.-H. Shin, D. Andreoli, J. Zhang, R. Xiao, Y.-F. Zhao, M. Kayyalha, L. Zhang, K. Wang, J. Zang, C. Liu, N. Samarth, M. H. W. Chan, and C.-Z. Chang, Concurrence of quantum anomalous Hall and topological Hall effects in magnetic topological insulator sandwich heterostructures, Nat. Mater. 1 (2020).

[13] J. C. Gallagher, K. Y. Meng, J. T. Brangham, H. L. Wang, B. D. Esser, D. W. McComb, and F. Y. Yang, Robust Zero-Field Skyrmion Formation in FeGe Epitaxial Thin Films, Phys. Rev. Lett. **118**, 027201 (2017).

[14] W. Wang, M. W. Daniels, Z. Liao, Y. Zhao, J. Wang, G. Koster, G. Rijnders, C.-Z. Chang, D. Xiao, and W. Wu, Spin chirality fluctuation in two-dimensional ferromagnets with perpendicular magnetic anisotropy, Nat. Mater. **18**, 1054 (2019).

[15] B. Huang, G. Clark, E. Navarro-Moratalla, D. R. Klein, R. Cheng, K .L. Seyler, D. Zhong, E. Schmidgall, M. A. McGuire, D. H. Cobden, W. Yao, D. Xiao, P. Jarillo-Herrero, and X. Xu, Layer-dependent ferromagnetism in a van der Waals crystal down to the monolayer limit, Nature (London) **546**, 270 (2017).

[16] C. Gong, L. Li, Z. Li, H. Ji, A. Stern, Y. Xia, T. Cao, W. Bao, C. Wang, Y. Wang, Z. Q. Qiu, R. J. Cava, S. G. Louie, J. Xia, and X. Zhang, Discovery of intrinsic ferromagnetism in two-dimensional van der Waals crystals, Nature (London) **546**, 265 (2017).

[17] S. Jiang, L. Li, Z. Wang, K. F. Mak, and J. Shan, Controlling magnetism in 2D CrI_3 by electrostatic doping, Nat. Nanotechnol. **13**, 549 (2018).

[18] T. Song, X. Cai, M.W.-Y. Tu, X. Zhang, B. Huang, N. P. Wilson, K. L. Seyler, L. Zhu, T. Taniguchi, K. Watanabe, M. A. McGuire, D. H. Cobden, D. Xiao, W. Yao, and X. Xu, Giant tunneling magnetoresistance in spin-filter van der Waals heterostructures, Science **360**, 1214 (2018).

[19] Y. Deng, Y. Yu, Y. Song, J. Zhang, N. Z. Wang, Z. Sun, Y. Yi, Y. Z. Wu, S. Wu, J. Zhu, J. Wang, X. H. Chen, and Y. Zhang, Gate-tunable room-temperature ferromagnetism in two-dimensional Fe_3GeTe_2, Nature (London) **563**, 94 (2018).

[20] W. Xing, L. Qiu, X. Wang, Y. Yao, Y. Ma, R. Cai, S. Jia, X. C. Xie, and W. Han, Magnon Transport in Quasi-Two-Dimensional van der Waals Antiferromagnets, Phys. Rev. X **9**, 011026 (2019).

[21] M. M. Otrokov, I. I. Klimovskikh, H. Bentmann, A. Zeugner, Z. S. Aliev, S. Gass, A. U. Wolter, A. V. Koroleva, D. Estyunin, and A. M. Shikin, Prediction and observation of the first antiferromagnetic topological insulator, Nature (London) **576**, 416 (2019).

[22] M. M. Otrokov, I. P. Rusinov, M. Blanco-Rey, M. Hoffmann, A. Y. Vyazovskaya, S. V. Eremeev, A. Ernst, P. M. Echenique, A. Arnau, and E. V. Chulkov, Unique Thickness-Dependent Properties of the van der Waals Interlayer Antiferromagnet $MnBi_2Te_4$ Films, Phys. Rev. Lett. **122**, 107202 (2019).

[23] J. Cui, M. Shi, H. Wang, F. Yu, T. Wu, X. Luo, J. Ying, and X. Chen, Transport properties of thin flakes of the antiferromagnetic topological insulator $MnBi_2Te_4$, Phys. Rev. B **99**, 155125 (2019).

[24] Y. Deng, Y. Yu, M. Z. Shi, J. Wang, X. H. Chen, and Y. Zhang, Quantum anomalous Hall effect in intrinsic magnetic topological insulator $MnBi_2Te_4$, Science **367**, 895 (2020).

[25] C. Liu, Y. Wang, H. Li, Y. Wu, Y. Li, J. Li, K. He, Y. Xu, J. Zhang, and Y. Wang, Robust axion insulator and Chern insulator phases in a two-dimensional antiferromagnetic topological insulator, Nat. Mat. **19**, 522 (2020).

[26] D. Zhang, M. Shi, T. Zhu, D. Xing, H. Zhang, and J. Wang, Topological Axion States in the Magnetic Insulator $MnBi_2Te_4$ with the Quantized Magnetoelectric Effect, Phys. Rev. Lett. **122**, 206401 (2019).

[27] Y. Gong, J. Guo, J. Li, K. Zhu, M. Liao, X. Liu, Q. Zhang, L. Gu, L. Tang, X. Feng, D. Zhang, W. Li, C. Song, L. Wang, P. Yu, X. Chen, Y. Wang, H. Yao, W. Duan, Y. Xu, S.-C. Zhang, X. Ma, Q.-K. Xue, and K. He, Experimental realization of an intrinsic magnetic topological insulator, Chin. Phys. Lett. **36**, 076801 (2019).

[28] J. Li, Y. Li, S. Du, Z. Wang, B.-L. Gu, S.-C. Zhang, K. He, W. Duan, and Y. Xu, Intrinsic magnetic topological insulators in van der Waals layered $MnBi_2Te_4$-family materials, Sci. Adv. **5**, eaaw5685 (2019).

[29] J. Ge, Y. Liu, J. Li, H. Li, T. Luo, Y. Wu, Y. Xu, and J. Wang, High-Chern-Number and High-Temperature Quantum Hall Effect without Landau Levels, Nat. Sci. Rev. nwaa1089 (2020).

[30] S. H. Lee, Y. Zhu, Y. Wang, L. Miao, T. Pillsbury, H. Yi, S. Kempinger, J. Hu, C. A. Heikes, P. Quarterman *et al.*, Spin scattering and noncollinear spin structure-induced intrinsic anomalous Hall effect in antiferromagnetic topological insulator $MnBi_2Te_4$, Phys. Rev. Research **1**, 012011 (2019).

[31] J. Q. Yan, S. Okamoto, M. A. McGuire, A. F. May, R. J. McQueeney, and B. C. Sales, Evolution of structural, magnetic, and transport properties in $MnBi_{2-x}Sb_xTe_4$, Phys. Rev. B **100**, 104409 (2019).

[32] J. Q. Yan, Q. Zhang, T. Heitmann, Z. Huang, K. Y. Chen, J. G. Cheng, W. Wu, D. Vaknin, B. C. Sales, and R. J. McQueeney, Crystal growth and magnetic structure of $MnBi_2Te_4$, Phys. Rev. Mater. **3**, 064202 (2019).

[33] S. V. Eremeev, M. M. Otrokov, and E. V. Chulkov, Competing rhombohedral and monoclinic crystal structures in $MnPn_2Ch_4$ compounds: An ab-initio study, J. Alloys Compd. **709**, 172 (2017).

[34] R. C. Vidal, A. Zeugner, J. I. Facio, R. Ray, M. H. Haghighi, A. U. B. Wolter, L. T. C. Bohorquez, F. Caglieris, S. Moser, T. Figgemeier *et al.*, Topological Electronic Structure and Intrinsic Magnetization in $MnBi_4Te_7$: A Bi_2Te_3 Derivative with a Periodic Mn Sublattice, Phys. Rev. X **9**, 041065 (2019).

[35] C. Hu, X. Zhou, P. Liu, J. Liu, P. Hao, E. Emmanouilidou, H. Sun, Y. Liu, H. Brawer, A. P. Ramirez, H. Cao, Q. Liu, D. Dessau, and N. Ni, A van der Waals antiferromagnetic topological insulator with weak interlayer magnetic coupling, Nat. Commun. **11**, 97 (2020).

[36] T. Murakami, Y. Nambu, T. Koretsune, G. Xiangyu, T. Yamamoto, C. M. Brown, and H. Kageyama, Realization of interlayer ferromagnetic interaction in $MnSb_2Te_4$ toward the magnetic Weyl semimetal state, Phys. Rev. B **100**, 195103 (2019).

[37] H. Weng, X. Dai, and Z. Fang, Topological semimetals predicted from first-principles calculations, J. Phys.: Condens. Matter **28**, 303001 (2016).

[38] See Supplemental Material at http://link.aps.org/supplemental/10.1103/PhysRevMaterials.4.064411 for more detailed discussion on this topic.

[39] J. Rodríguez-Carvajal, Recent advances in magnetic structure determination by neutron powder diffraction, Physica B **192**, 55 (1993).

[40] B. H. Toby and R. B. Von Dreele, GSAS-II: The genesis of a modern open-source all purpose crystallography software package, J. Appl. Crystallogr. **46**, 544 (2013).

[41] G. Gandolfi, Discussion upon methods to obtain X-ray "powder patterns" from a single crystal, Miner. Petrogr. Acta **13**, 67 (1967).

[42] N. Nagaosa, J. Sinova, S. Onoda, A. H. MacDonald, and N. P. Ong, Anomalous Hall effect, Rev. Mod. Phys. **82**, 1539 (2010).

[43] Y. Moritomo, Y. Tomioka, A. Asamitsu, Y. Tokura, and Y. Matsui, Magnetic and electronic properties in hole-doped manganese oxides with layered structures: $La_{1-x}Sr_{1+x}MnO_4$, Phys. Rev. B **51**, 3297 (1995).

[44] J. S. Gardner, M. J. P. Gingras, and J. E. Greedan, Magnetic pyrochlore oxides, Rev. Mod. Phys. **82**, 53 (2010).

[45] J. Wu and C. Leighton, Glassy ferromagnetism and magnetic phase separation in $La_{1-x}Sr_xCoO_3$, Phys. Rev. B **67**, 174408 (2003).

[46] J. D. Bocarsly, C. Heikes, C. M. Brown, S. D. Wilson, and R. Seshadri, Deciphering structural and magnetic disorder in the chiral skyrmion host materials $Co_xZn_yMn_z$ $(x + y + z = 20)$, Phys. Rev. Mater. **3**, 014402 (2019).

[47] J. P. Gaspard and R. Ceolin, Hume-Rothery rule in V–VI compounds, Solid State Commun. **84**, 839 (1992).

[48] Y. S. Hor, P. Roushan, H. Beidenkopf, J. Seo, D. Qu, J. G. Checkelsky, L. A. Wray, D. Hsieh, Y. Xia, S. Y. Xu, D. Qian, M. Z. Hasan, N. P. Ong, A. Yazdani, and R. J. Cava, Development of ferromagnetism in the doped topological insulator $Bi_{2-x}Mn_xTe_3$, Phys. Rev. B **81**, 195203 (2010).

[49] J. S. Lee, A. Richardella, D. W. Rench, R. D. Fraleigh, T. C. Flanagan, J. A. Borchers, J. Tao, and N. Samarth, Ferromagnetism and spin-dependent transport in *n*-type Mn-doped bismuth telluride thin films, Phys. Rev. B **89**. 174425 (2014).

[50] D. Vaknin, D. M. Pajerowski, D. L. Schlagel, K. W. Dennis, and R. J. McQueeney, Two-dimensional ordering and collective magnetic excitations in the dilute ferromagnetic topological insulator $(Bi_{0.95}Mn_{0.05})_2Te_3$, Phys. Rev. B **99**, 220404 (2019).

[51] D. Boldrin and A. S. Wills, Anomalous Hall effect in geometrically frustrated magnets, Adv. Condens. Matter Phys. **2012**, 12 (2012).

[52] H. Kawamura, Anomalous Hall Effect as a Probe of the Chiral Order in Spin Glasses, Phys. Rev. Lett. **90**, 047202 (2003).

[53] H. Chen, Q. Niu, and A. H. MacDonald, Anomalous Hall Effect Arising from Noncollinear Antiferromagnetism, Phys. Rev. Lett. **112**, 017205 (2014).